Parameter estimation in fluid flow models from aliased velocity measurements

Garay, Jeremías; Nolte, David; Löcke, Miriam; Bertoglio, Cristóbal

Published in:
Inverse problems

DOI:
10.1088/1361-6420/ac836e

Publication date:
2022

Parameter estimation in fluid flow models from aliased velocity measurements

OPEN ACCESS
IOP Publishing
Inverse Problems
Inverse Problems **38** (2022) 095002 (21pp)
https://doi.org/10.1088/1361-6420/ac836e

Parameter estimation in fluid flow models from aliased velocity measurements

Jeremías Garay[1], David Nolte[1,2], Miriam Löcke[1] and Cristóbal Bertoglio[1,*]

[1] Bernoulli Institute, University of Groningen, The Netherlands
[2] Department for Fluid Dynamics, Technical University of Berlin, Germany

E-mail: c.a.bertoglio@rug.nl

Received 14 January 2022, revised 10 June 2022
Accepted for publication 22 July 2022
Published 11 August 2022

Abstract

Parameter estimation in blood flow models from measured velocity data—as e.g. velocity-encoded MRI—is a key step for patient-specific hemodynamic analysis. However, velocity encoding suffers from competing noise and aliasing artifacts, which negatively impact the parameter estimation results. The aim of this work is to propose a new inverse problem formulation capable of tackling aliased and noisy velocity MRI measurements in parameter estimation in flows. The formulation is based on a modification of the quadratic cost function for velocity measurements. This allows for a correct parameter estimation when they have influence on the whole measurement domain, in spite of aliasing artifacts. The new inverse problem can be solved numerically using any standard solver, and we show how a popular sequential approach can be applied. Numerical results in an aortic flow show robust parameter estimation for velocity encoding ranges until 30% of the maximal velocity of the problem, while the standard inverse problem fails already for any encoding velocity smaller than the true one. Moreover, the parameter estimation results are even improved for reduced velocity encoding ranges when using the new cost function. The presented approach allows therefore for great flexibility in personalization of blood flows models from MRI data commonly encountered in the clinical context.

Keywords: blood flows modeling, phase-contrast MRI, velocity aliasing, Windkessel model, Kalman filtering

(Some figures may appear in colour only in the online journal)

*Author to whom any correspondence should be addressed.

1. Introduction

In blood flows, the personalization of spatially distributed (i.e. 3D) models is a key step in performing predictive patient-specific simulations. Such a step relies on the formulation and numerical solution of inverse problems using clinical data, namely medical images for measuring both anatomy and function of the vasculature. However, full-scale hemodynamics simulations of the complete vasculature will remain unfeasible for the foreseeable future [1]. Therefore, detailed 3D computations are restricted to particular regions of interest of the cardiovascular system and have to be carried out within truncated computational domains.

Lumped parameter models (LPM) can efficiently deliver realistic boundary conditions, accounting for the effects of the omitted parts of the vascular system. LPMs group the spatially distributed vascular system into so-called '0D' compartments, over which the conservation laws are averaged to obtain ordinary differential equations (ODE) modeling the flow rate and the average pressure.

The most popular 0D model choice is the *three-element Windkessel model*, which contains as physical parameters the vessel compliance, the distal resistance and the proximal resistance [2].

In the context of 3D–0D coupled models, the personalization typically relies on estimating those 0D model parameters at each outlet boundary of the 3D model from velocity (and eventually pressure) data using non-linear least-squares approaches solved via variational [3] or sequential [4, 5] methods.

The gold standard for distributed blood flow velocity measurements in the clinical context is phase-contrast magnetic resonance imaging (PC-MRI) [6, 7]. However, PC-MRI presents important artifacts, noise and velocity aliasing being the most important ones. When personalizing the models with such data, not taking these artifacts into account can lead to important inaccuracies in the blood flow model personalization.

MRI applies sequences of spatially and temporally varying magnetic vector fields, inducing a magnetic response from the sample, i.e., a magnetization vector in which the spatial location is encoded. The anatomical images are created from the norm of the magnetization vector, which depends on the type of tissue being imaged (blood, muscle, bone, air, etc). The phase of the magnetization vector can encode the blood velocity by properly choosing the magnetic gradients using [8, 9].

However, the phase can only be measured in the half-open interval $[-\pi, \pi)$ and phase wraps (abrupt jumps of $\pm 2\pi$) occur if the encoded phase exceeds those limits. The velocity limit—or *venc*—is fixed by the scanner operator before the measurement. Unfortunately, selecting a large *venc* leads to poor quality images since—for a given signal-to-noise-ratio (SNR) in the magnitude image—the 'velocity-to-noise-ratio' (VNR) is inversely proportional to the *venc*.

While unwrapping methods have been reported, they also perturbe the velocity measurements [10–12] possibly leading to faulty parameter estimations.

Therefore, in this work we introduce a new but straightforward inverse problem formulation in order to effectively account for aliased velocity data. This is accomplished by a generalization of the cost function using the fact that phase-contrast problem accounts for multiple periodic solutions. This new formulation is naturally derived from the phase-contrast problem with the complex MRI signal as input.

The remainder of this paper is structured as follows. In section 2 we introduce the mathematical model (3D–0D problem), including the 3D–0D coupling scheme formulation and

numerical results. In section 3 the measurement model is detailed, and examples of aliased and noisy measurements are presented. We also include unwrapping approaches that serve to partially remove aliasing artifacts. Then, in section 4 the standard and new inverse problem formulations are introduced, and numerical results shown. Finally, section 5 gives some conclusions.

2. The forward problem

2.1. The mathematical model

Let $\Omega \subset \mathbb{R}^3$ be a domain standing for the lumen of the vessel, represented in figure 1, with its boundary $\partial\Omega$ sub-divided as follows:

$$\partial\Omega = \Gamma_{\text{in}} \cup \Gamma_{\text{w}} \cup \left(\cup_{\ell=1}^{K} \Gamma_\ell\right),$$

where Γ_{in} is the inlet boundary (proximal to the heart), Γ_{w} the arterial wall and $\Gamma_1, \ldots, \Gamma_K$ the K outlet boundaries. We consider then in this domain the incompressible Navier–Stokes equation for the velocity $\mathbf{u}(\mathbf{x}, t) \in \mathbb{R}^3$ and pressure $p(\mathbf{x}, t) \in \mathbb{R}$:

$$\begin{cases} \rho\dfrac{\partial \mathbf{u}}{\partial t} + \rho(\mathbf{u}\cdot\nabla)\mathbf{u} - \mu\Delta\mathbf{u} + \nabla p = 0 & \text{in} \quad \Omega \times [0,T] \\ \nabla\cdot\mathbf{u} = 0 & \text{in} \quad \Omega \times [0,T] \\ \mathbf{u} = \mathbf{u}_{\text{inlet}} & \text{on} \quad \Gamma_{\text{in}} \times [0,T] \\ \mathbf{u} = \mathbf{0} & \text{on} \quad \Gamma_{\text{w}} \times [0,T] \\ \mu\dfrac{\partial \mathbf{u}}{\partial n} - p\mathbf{n} = -P_\ell(t)\mathbf{n} & \text{on} \quad \Gamma_\ell \times [0,T], \quad \ell = 1,\ldots,K, \end{cases} \tag{1}$$

where ρ is the density and μ the dynamic viscosity of the fluid and $P_\ell(t)$ is given by the *three-element Windkessel* model [2]:

$$\begin{cases} P_\ell = R_{p,\ell}\, Q_\ell + \pi_\ell \\ Q_\ell = \displaystyle\int_{\Gamma_\ell} \mathbf{u}\cdot\mathbf{n} \\ C_{d,\ell}\dfrac{\mathrm{d}\pi_\ell}{\mathrm{d}t} + \dfrac{\pi_\ell}{R_{d,\ell}} = Q_\ell. \end{cases} \tag{2}$$

In this model, $R_{p,\ell}$ and $R_{d,\ell}$ represent the resistance of the vasculature proximal and distal to Γ_ℓ, respectively, and $C_{d,\ell}$ the compliance of the distal vessels. $\mathbf{n}$ is the exterior normal vector of $\partial\Omega$. Note that substituting the first equation of (2) into the third leads to the classical formulation of the model with a single equation coupling P, Q and its time-derivatives. The initial conditions $\mathbf{u}(\mathbf{x}, 0), \pi_1(0), \ldots, \pi_K(0)$ are also given.

The other boundary conditions are set as follows. At Γ_{in} a pulsatile plug flow was imposed setting the velocity to be:

$$\mathbf{u}_{\text{inlet}} = -Uf(t)\ \mathbf{n},$$

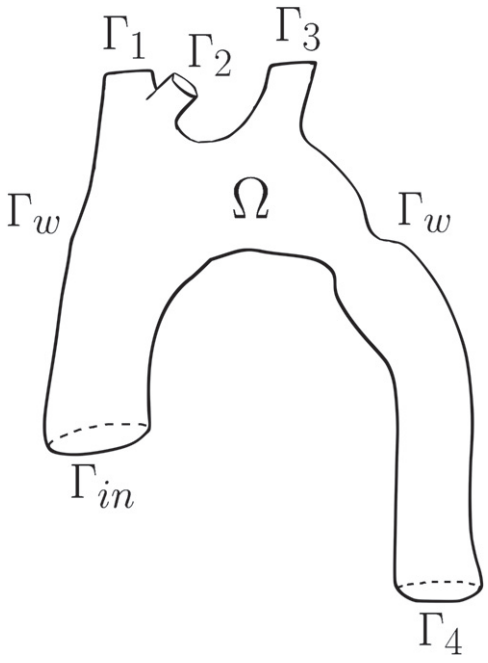

Figure 1. 3D aortic model geometry coupled with Windkessel models.

where U is a constant amplitude and $f(t)$ is a given waveform defined as:

$$f(t) = \begin{cases} \sin\left(\dfrac{\pi t}{T}\right) & \text{if } t \leqslant T \\ \dfrac{\pi}{T}(t-T)\mathrm{e}^{-\kappa(t-T)} & \text{if } T_c > t > T \end{cases}.$$

Here, T is the opening-time of the valve, T_c the total duration of the cardiac cycle and $1/\kappa$ represents the typical time for the closing of the valve.

The Windkessel constants were tuned by hand in order to have a standard physiological flow regime to achieve approximately $70\%/30\%$ split in the peak flow rate between the descending aorta and supra-aortic branches [13, 14]. For the numerical values of these constants, the physical parameters of the fluid and the constants of the Windkessel models see table 1.

2.2. A modified semi-implicit 3D–0D coupling scheme

For the spatial discretization, let be Ω_h the representation of the vessel domain by a certain mesh supplied by a suitable triangulation with a the level of refinement h. We consider the Sobolev subspace: $H^1_Y(\Omega_h) = \{w \in H^1(\Omega_h) : w = 0 \text{ on } Y \subset \partial\Omega\}$. Additionally, considering continuous Lagrange finite elements we can define the following spaces for the velocity $\mathbf{u}$ and the pressure p, respectively:

$$V_{Y,h} = [\mathbb{P}_1(\Omega_h)]^3 \cap [H^1_Y(\Omega_h)]^3 \quad , \quad Q_h = \mathbb{P}_1(\Omega_h) \cap H^1(\Omega_h). \tag{3}$$

For the time discretization, and for the purpose of computational efficiency, we solve problem (1) using a Chorin–Temam scheme with a backward Euler scheme for the time

Table 1. Physical parameters and numerical values of the three-element Windkessel parameters for every outlet.

Parameter				Value
ρ (gr $\cdot$ cm^3)				1.2
μ (P)				0.035
U (cm $\cdot$ s^{-1})				75
T_c (s)				0.80
T (s)				0.36
κ (s^{-1})				70
	Γ_1	Γ_2	Γ_3	Γ_4
R_p (dyn $\cdot$ s $\cdot$ cm^{-5})	480	520	520	200
R_d (dyn $\cdot$ s $\cdot$ cm^{-5})	7200	11 520	11 520	4800
C (dyn^{-1} $\cdot$ cm^5)	4×10^{-4}	3×10^{-4}	3×10^{-4}	4×10^{-4}

derivative. In simple terms, the full equation is split into sequential sub-problems, see [15] for a review. The first sub-problem solves for the so-called *tentative* velocity, which takes into account the first equation in problem (1) but taking the pressure gradient explicit in time, hence not strictly enforcing the incompressibility. The second sub-problem solves for the pressure from the tentative velocity. The final step computes a *corrected* velocity using the gradient pressure, enforcing (global) mass conservation.

Problem (2) is discretized using a backward Euler approximation:

$$\begin{cases} \pi_\ell^n = \alpha_\ell \pi_\ell^{n-1} + \beta_\ell Q_\ell^n, \\ P_\ell^n = \gamma_\ell Q_\ell^n + \alpha_\ell \pi_\ell^{n-1}, \end{cases} \tag{4}$$

with $\alpha_\ell = R_{d,\ell} C_{d,\ell} / (R_{d,\ell} C_{d,\ell} + \tau)$, $\beta_\ell = R_{d,\ell}(1 - \alpha_\ell)$ and $\gamma_\ell = R_{p,\ell} + \beta_\ell$.

The coupling between the 3D and 0D models depends on the choice of Q_ℓ in the right-hand-side of (4), namely, if Q_ℓ is computed from the tentative or corrected velocity field [16]. Using the tentative velocity leads to an explicit algorithm where all quantities used in equation (4) are known at the moment of the pressure projection step where P_ℓ is used. Using the corrected velocity leads to an implicit coupling of the Windkessel and the pressure projection problem since the flow rate Q_ℓ is also an unknown at this step. Hence this approach is termed as *semi-implicit*.

Even though the explicit approach is the most straightforward to implement, it is the semi-implicit strategy that can be proven as unconditionally stable. For more details of these two strategies see [16]. Unconditional stability is crucial in inverse problems—and in particular in Kalman filtering—since the physical parameters of the model are varied during the computation.

However, the original semi-implicit Chorin–Temam strategy has some implementation difficulties requiring constraining the solution spaces of the pressure to be constant on the outlets, possibly making its implementation difficult depending on the features of the code in use [16]. To avoid such constraints, in this work we present a modified version, see algorithm 1. There, we only penalize the pressure's tangent derivative (third term in equation (6)) and then we couple the 3D and 0D models using the outlet's average pressure.

The modified scheme can also be analyzed in terms of its time stability applying the analysis for the original semi-implicit method from [16] straightforwardly. Hence, this leads also to an unconditionally stable method.

Algorithm 1. Fractional step algorithm with a modified semi-implicit Windkessel model coupling.

Given the initial conditions $\mathbf{u}^0 = \mathbf{u}(0) \in V_{\Gamma_w,h}$ and $\pi_1^0, \ldots, \pi_N^0 \in \mathbb{R}$, perform for $n > 0$, with $t^n = n\tau$:

1. Viscous step: find the tentative velocity $\tilde{\mathbf{u}}^n \in V_{\Gamma_w,h}$ such that:

$$\begin{cases} \tilde{\mathbf{u}}^n_{\Gamma_{\text{in}}} = \mathbf{u}_{\text{inlet}}(t^n) \\ \frac{\rho}{\tau}(\tilde{\mathbf{u}}^n, \mathbf{v})_{\Omega_h} + \rho(\mathbf{u}^{n-1} \cdot \nabla \tilde{\mathbf{u}}^n, \mathbf{v})_{\Omega_h} + \frac{\rho}{2}((\nabla \cdot \mathbf{u}^{n-1})\tilde{\mathbf{u}}^n, \mathbf{v})_{\Omega_h} + (\delta \mathbf{u}^{n-1} \cdot \nabla \tilde{\mathbf{u}}^n, \mathbf{u}^{n-1} \cdot \nabla \mathbf{v})_{\Omega_h} \\ +2\mu(\epsilon(\tilde{\mathbf{u}}^n), \epsilon(\mathbf{v}))_{\Omega_h} + \sum_{\ell=1}^{K} \frac{\rho}{2}|\mathbf{u}^{n-1} \cdot \mathbf{n}|_-(\tilde{\mathbf{u}}^n, \mathbf{v})_{\Gamma_\ell} = \frac{\rho}{\tau}(\mathbf{u}^{n-1}, \mathbf{v})_{\Omega_h} \end{cases} \tag{5}$$

for all $\mathbf{v} \in V_{\Gamma_{\text{in}} \cup \Gamma_w,h}$, and $|x|_-$ denoting the negative part of x.

2. Projection-Windkessel step: compute $\tilde{Q}^n = \int_{\Gamma_\ell} \tilde{\mathbf{u}}^n \cdot \mathbf{n}$. Find $p^n \in Q_h$ such that:

$$\begin{aligned} &\tfrac{\tau}{\rho}(\nabla p^n, \nabla q)_{\Omega_h} + \textstyle\sum_{\ell=1}^{K} \frac{\overline{p^n}_{\Gamma_\ell}\, \overline{q}_{\Gamma_\ell}}{\gamma_\ell} + \epsilon \sum_{\ell=1}^{K} (\mathcal{T}(\nabla p^n), \\ &\mathcal{T}(\nabla q))_{\Gamma_\ell} = \textstyle\sum_{\ell=1}^{K} \left(\tilde{Q}^n + \frac{\alpha_\ell \pi_\ell^{n-1}}{\gamma_\ell} \right) \overline{q}_{\Gamma_\ell} - (\nabla \cdot \tilde{\mathbf{u}}^n, q)_{\Omega_h}, \end{aligned} \tag{6}$$

for all $q \in Q_h$ and with $\overline{(\cdot)}_{\Gamma_\ell} = \frac{1}{\text{Area}(\Gamma_\ell)} \int_{\Gamma_\ell} (\cdot) \mathrm{d}s$ and $\mathcal{T}(\mathbf{f}) = \mathbf{f} - (\mathbf{f} \cdot \mathbf{n})\mathbf{n}$.

3. Velocity correction step: find $\mathbf{u}^n \in [L^2(\Omega_h)]^3$ such that:

$$(\mathbf{u}^n, \mathbf{v})_{\Omega_h} = \left(\tilde{\mathbf{u}}^n - \tfrac{\tau}{\rho} \nabla p^n, \mathbf{v} \right)_{\Omega_h}$$

for all $\mathbf{v} \in [L^2(\Omega_h)]^3$

4. Update-Windkessel step: set $P_\ell^n = \overline{p^n}_{\gamma_\ell}$ and compute $\pi_\ell^n \in \mathbb{R}$ as:

$$\pi_\ell^n = \left(\alpha_\ell - \tfrac{\alpha_\ell \beta_\ell}{\gamma_\ell} \right) \pi_\ell^{n-1} + \tfrac{\beta_\ell}{\gamma_\ell} P_\ell^n, \ \ell = 1, \ldots, K$$

Note also that at the viscous step (equation (1)) several convection-related stabilizations are also added, as backflow [17], Temam and streamline-diffusion (i.e. SUPG stabilization with the formula for the stabilization parameter δ taken from [18]).

Note that at the projection step of algorithm 1, the non-local terms at each outlet can be incorporated into the sparse representation of the Laplacian. In order to do that, we use a low rank update of the form $M = A + VDV'$, where $A \in \mathbb{R}^{N \times N}$ is the matrix of the discrete Laplacian, $V \in \mathbb{R}^{N \times K}$ is the pressure boundary support defined by the term $\overline{p^n}_{\Gamma_\ell}$ (see second step of algorithm 1) and $D \in \mathbb{R}^{K \times K}$ a diagonal matrix containing weights for the K Windkessel outlets. In our implementation, the matrix M is never explicitly formed, the low rank update being directly handled the update handled directly by the GMRES solver of the PETSc library.

2.3. Reference numerical solution

The initial conditions were set as $\mathbf{u}^0 = \mathbf{0}$ and $\pi_\ell^0 = 85$ mm Hg for $\ell = 1, \ldots, K$. The values of π_ℓ^0 corresponds to approximately the periodic state of the 3D–0D system.

Concerning the numerical setup, we solve the fractional step system using the algorithm 1. The computational domain corresponds to an aorta with a coarctation in the descending part, with a total streamwise length of 11.2 cm and meshed with 2752 064 tetrahedrons and 510 755 vertices. The time step is set as $\tau = 0.001$ s with a total run time of 0.8 s. The ϵ parameter for the pressure gradient penalization at every outlet was set to 20, chosen as the smallest possible value such that the results appear to be visually insensitive to ϵ.

Figure 2 shows the results for the velocity field at peak systole, the flow rates and pressures at the inlet and outlet boundaries.

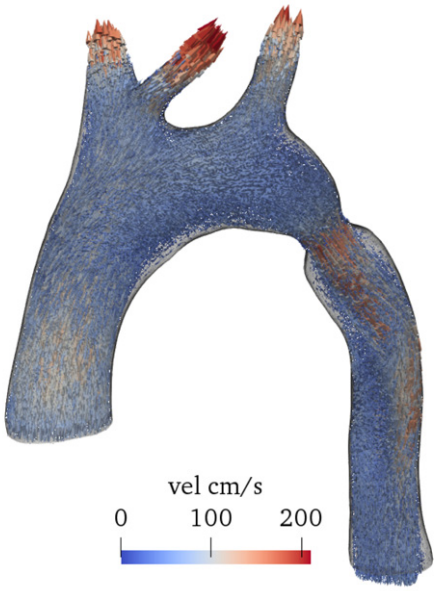

(a) Peak systole reference velocity field undesampled $\times 4$ in order to ease the visualization

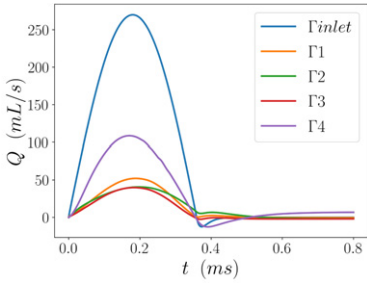

(b) Flow rates at the boundaries

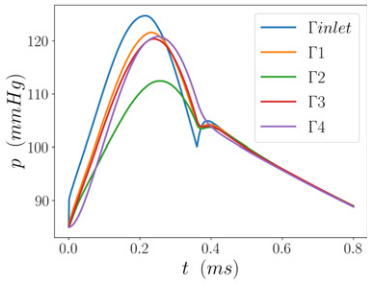

(c) Average pressures at the boundaries

Figure 2. Velocity field and outlet pressures and flow rates obtained with algorithm 1 and parameters from section 2.3.

3. The measurements

3.1. Phase-contrast and aliasing in a nutshell

Let us denote by u_{true} the velocity field at a point in space and time. In PC-MRI, the transverse (complex) *magnetization* signal is given by the model:

$$M^u_{\text{meas}} = C\,\exp\big(i(\phi^0 + \pi u_{\text{true}}/venc)\big) + \varepsilon^u \tag{7}$$

with ϕ^0 the so-called *background* phase which depends on, among other quantities, spatial inhomogeneities of magnetic gradients, and C corresponds to the magnitude (typical showing tissue variations and therefore use for anatomical imaging). As usually assumed in MRI [19], $\varepsilon^u \in \mathbb{C}$ is set to be a zero-mean Gaussian measurement noise. The only quantity known *a priori* is the *velocity encoding value* or *venc*, which is set by the MRI scanner operator determining the shape of the motion encoding gradients.

Since ϕ^0 is unknown, in order to recover an estimate of u_{true} from magnetization measurements, PC-MRI involves an additional measurement. This is typically done by turning off the motion encoding gradient leading to the model:

$$M^0_{\text{meas}} = C\,\exp\big(i(\phi^0)\big) + \varepsilon^0. \tag{8}$$

The velocity is then estimated from the resulting division of the magnetizations by:

$$u_{\text{meas}} = \frac{\angle\left(M^{u}_{\text{meas}}/M^{0}_{\text{meas}}\right)}{\pi} venc \tag{9}$$

with $\angle$ denoting the phase of the complex number to which it is applied.

For a high signal-to-noise ratio (SNR) in the magnetization measurements, it can be shown that the velocity-to-noise ratio of u_{meas} can be written as [19]:

$$\text{VNR} = \frac{\pi}{\sqrt{2}} \frac{\text{SNR}}{venc}$$

the choice of the *venc* parameter being crucial for controlling the VNR. However, the *venc* defines the range at which velocity data can be encoded: the phase can only be measured in the interval $[-\pi, \pi)$. Therefore, *velocity aliasing* occurs when $|venc| < |u_{\text{true}}|$, i.e. the estimated velocity will be $u_{\text{true}} - 2j \cdot venc$ instead of u_{true}, with $j \in \mathbb{Z}$ depending on how much smaller $|venc|$ is with respect to $|u_{\text{true}}|$.

Note that this is a localized artifact—i.e. specific to some voxels and time instants—since u_{true} varies in space and time, while the *venc* does not. Therefore, velocity unwrapping algorithms have been developed by assuming that the true velocity field is smooth in space [10, 20, 21], time [11, 22] or both [12, 23]. Nevertheless, the unwrapped image appears distorted for realistic VNRs, and specially when the aliased regions are large or include multiple wraps (i.e. when $|j| > 1$).

Alternatively, voxelwise motion reconstructions using dual-encoding strategies have been proposed in PC-MRI which are based on unwrapping low *venc* data by exploiting high *venc* data [24–26]. Those methods are performed at each voxel and time instant independently and therefore they do not assume or enforce smoothness of the velocity-encoded phase field. Such approaches have, however, the cost of additional measurements.

The practical consequence of the trade-off between VNR and aliasing is that the scanner operator needs to select—by trial and error during the MRI scan—the value of *venc* to maximize VNR and to avoid aliasing. This leads to increased patient's examination time.

3.2. Measurement generation on the reference numerical solution

We simulated a PC-MRI acquisition on the *update* velocity solution $\mathbf{u}^0, \mathbf{u}^1, \ldots$ using algorithm 1 and the physical parameter values in section 2.3 leading to the solution shown in figure 2.

As the measurement domain ω_H, a rectangular mesh of hexahedra was generated, covering the complete Ω_h in that plane, with elements size $2 \times 2 \times 2$ mm^3. The original (i.e. simulation) mesh Ω_h and the slice mesh ω_H are shown in figure 3.

Then, the velocity fields $\mathbf{u}^0 \cdot \mathbf{d}, \mathbf{u}^1 \cdot \mathbf{d}, \ldots$ were interpolated onto ω_H using $\mathbb{P}_1$-Lagrange interpolation, with $\mathbf{d}$ the foot-head direction. For the purpose of the inverse problem solution, let us denote the operator performing component-selection together with the interpolation $\mathcal{H} : [H_1(\Omega_h)]^3 \to \mathbb{R}^m$, with m the number of elements of ω_H.

We also undersampled the velocity field in time to 0.03 s leading to $N_T = 28$ measurements per cardiac cycle.

Magnetization measurements, and subsequently (aliased) velocity measurements were created using equations (7)–(9) on each velocity value of the spatio-temporally undersampled velocities.

The reference phase was arbitrary set as: $\phi^0 = 7.5 \times 10^{-2}$ rad and constant for all nodes. The noise in the magnetization was applied such that a SNR of 15 dB in the complex magnetization was obtained. Moreover, three *venc* values as the 120%, 70% and 30% of the maximum

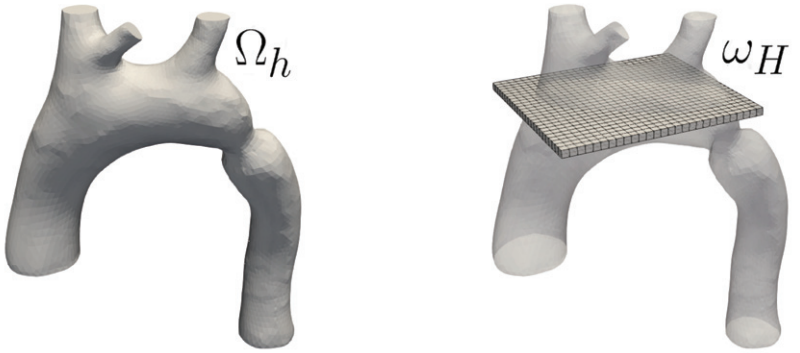

(a) Mesh Ω_h used for the solution of the forward problems

(b) Mesh ω_H used to represent the measurements

Figure 3. Simulations and measurement meshes.

reference velocity were chosen, resulting in the values of 115, 67 and 28 cm s^{-1}, respectively. This leads to 0, 1 and 2 wraps in the velocity field, respectively.

The values of u_{meas} for all measured spatial and time points are then grouped into a set of arrays $Z^k \in \mathbb{R}^m$, $k = 1, \ldots, N_T$.

Figures 4(b)–(d) show u_{meas} at peak systole for the different values of *venc* at the in-plane resolution of 2×2 mm^2. The reference slice is depicted in figure 4(a). As *venc* decreases the velocity-to-noise ratio improves since the noise in the magnetization remains of the same amplitude for all *venc* values. However, aliasing starts being visible, specially in zones with higher velocities as in the coarctation and at the supra-aortic outlets.

Figures 4(h), (i) and (j) show histograms for each measurement set, computed from velocity measurements at the initial time step. First, it can be seen that in spite of the nonlinear transformation from magnetization to velocity (see equation (9)), the noise in the velocity presents a Gaussian distribution. Moreover, it can be confirmed that the standard deviation of the velocity decreases with the *venc*.

3.3. Velocity unwrapping

Let us denote the true phase difference ϕ and the (possibly) wrapped phase difference $\phi_{\text{w}} = (u_{\text{meas}}/venc)\pi \in [-\pi, \pi)$ given by equation (9). The relationship between both can be represented as

$$\phi(x,t) = \phi_{\text{w}}(x,t) + 2\pi n(x,t) \tag{10}$$

where $n(x,t)$ is an integer function describing the number of wraps at the spatio-temporal position (x,t) since the *venc* is constant for the whole images but not the velocity.

Phase unwrapping can be performed in a number of different ways by assuming regularity in the spatial [10, 20, 21] or the temporal dimension [11, 22, 27] or both [12, 23]. Here we will apply temporal unwrapping since it has shown the best results in the measurement sets used in this work.

Temporal phase unwrapping has first been introduced in [27]. This method assumes that the velocity difference between two adjacent timeframes is less than *venc*, therefore relying on that the phase only varies slowly in time or that the temporal resolution is high enough.

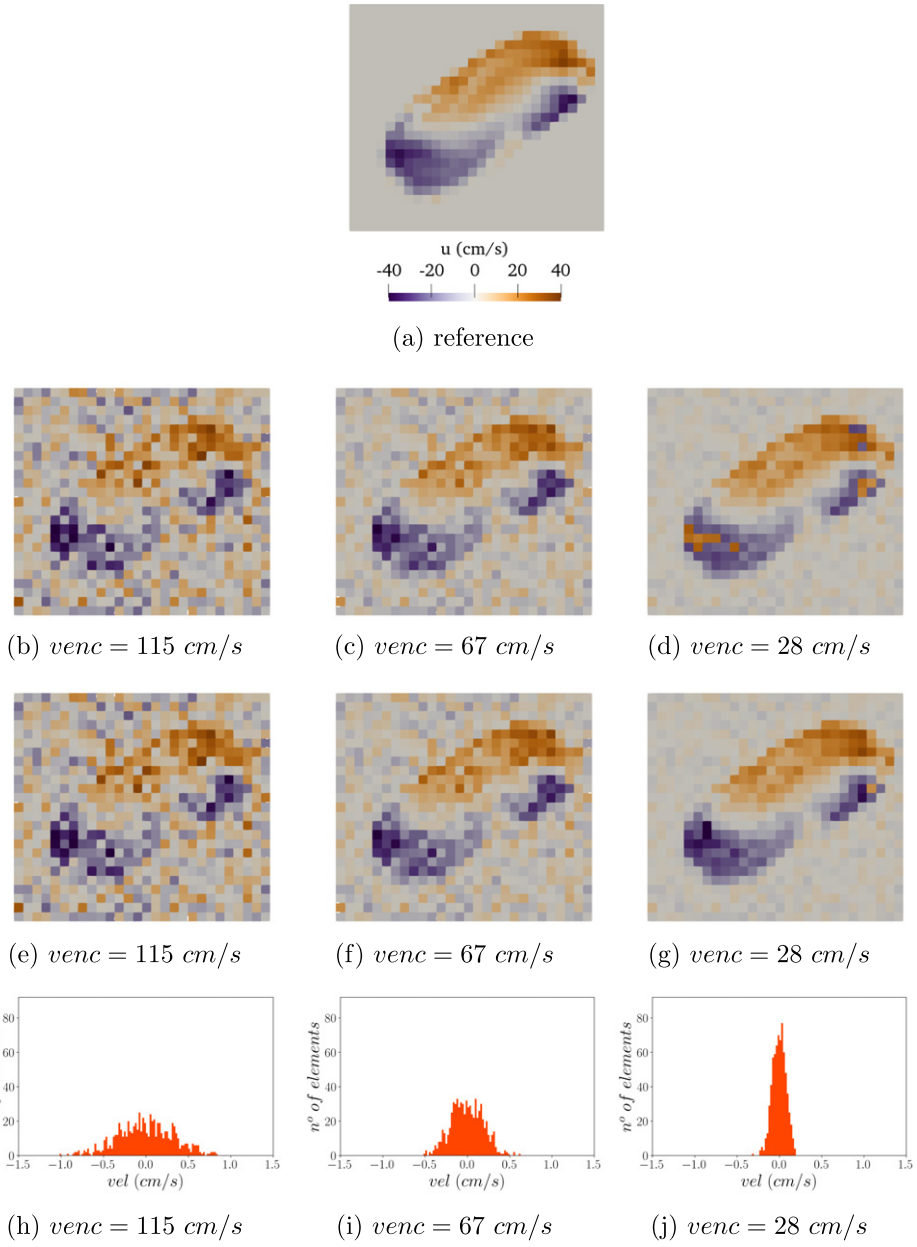

(a) reference

(b) $venc = 115\ cm/s$ (c) $venc = 67\ cm/s$ (d) $venc = 28\ cm/s$

(e) $venc = 115\ cm/s$ (f) $venc = 67\ cm/s$ (g) $venc = 28\ cm/s$

(h) $venc = 115\ cm/s$ (i) $venc = 67\ cm/s$ (j) $venc = 28\ cm/s$

Figure 4. u_{meas} distributions for different *venc* values. (a) Reference slice. (b)–(d) Values of the velocity for different *venc* at time $t = 0.36$ s. (e)–(g) Unwrapped velocity measurements at $t = 0.36$ s. (h)–(j) Histograms of the velocity at the initial timestep within the whole aorta.

Given a time series of N_T measured phase maps $\phi_{\text{w}}(x, t_1), \ldots, \phi_{\text{w}}(x, t_{N_T})$, the set of differential phase maps is computed as

$$D_i(x, t_i) = \phi_{\text{w}}(x, t_i) - \phi_{\text{w}}(x, t_{i-1}), \quad i = 2, \ldots, N_T.$$

According to the assumption, these differential maps do not contain any phase wraps of their own. Therefore any absolute value greater than π has to be the result of a phase wrap occurring in one of the phase maps.

To regain the 'correct' differential value, the differential phase maps are wrapped back into the range $[-\pi, \pi)$ by calculating

$$D_i^*(x) = D_i(x) + 2\pi n(x, t_i)$$

where $n(x, t_i)$ is an integer such that $D_i^*(x) \in [-\pi, \pi)$. Once the wrap-free differential phase maps have been computed, the unwrapped phase maps are calculated by integrating over the differential maps, starting at a reference timeframe which does not contain any wrapped voxels. For this reference frame a timeframe at beginning of diastole is selected, as it is the least likely to have aliasing.

The unwrapped phase ϕ_{uw} with a reference phase image $\phi_{\mathrm{w}}(x, t_r)$ at time t_r is then computed as

$$\phi_{\mathrm{uw}}(x, t_j) = \begin{cases} \phi_{\mathrm{w}}(x, t_r) + \displaystyle\sum_{i=r+1}^{j} D_i^*(x) & \text{for } j > r \\ \phi_{\mathrm{w}}(x, t_r) - \displaystyle\sum_{i=j+1}^{r} D_i^*(x) & \text{for } j < r \\ \phi_{\mathrm{w}}(x, t_r) & \text{for } j = r \end{cases}.$$

Finally, the unwrapped velocity image is given by $u_{\mathrm{uw}}(x, t_i) = (\phi_{\mathrm{w}}(x, t_i)/\pi)venc, i = 1, \ldots, N_T$.

Figures 4(e)–(g) shows the results of the unwrapping algorithms applied at time 0.36 s

4. The inverse problem

4.1. Parameters to be estimated

We first justify the parameters chosen for the estimation from velocity measurements $Z^1, \ldots, Z^N$, which will remain the same for the cases with and without aliasing in the data.

It is well known in computational hemodynamics that the flow split is given by the ratios of the total resistances between outlets. Also, in the absence of pressure measurements, not all the resistances of the system can be determined uniquely from velocity measurements only.

Moreover, the total resistance is dominated by the distal resistance for realistic values of these parameters, i.e. $R_{p,\ell} \ll R_{d,\ell}$. Including additional parameters like the compliances $C_{d,\ell}$ would also require pressure measurements as presented e.g. in [5].

Hence, for the parameters to be estimated from the velocity measurements, we consider in this work the amplitude velocity at the inlet, U, and the Windkessel distal resistances $R_{d,1}, \ldots, R_{d,K-1}$. The choice of fixing $R_{d,K}$ is arbitrary, as it could have been any of the other resistances.

4.2. The classical inverse problem from velocities

Let us summarize the set of parameters to be estimated as $\theta \in \mathbb{R}^p$. The parameter estimation problem can be tackled using a Bayesian framework, i.e. to minimize the functional

$$\hat{\theta} = \arg\min_{\theta} \frac{1}{2}\|\theta - \theta_0\|^2_{P_0^{-1}} + \frac{1}{2\sigma_z^2}\sum_{k=1}^{N_T}\sum_{s=1}^{m}([Z^k - \mathcal{H}(\mathbf{u}_\theta^k)]_s)^2 \tag{11}$$

where $\mathbf{u}_\theta^k$ and θ are related through the forward model summarized in algorithm 1. The s index denotes sum over all voxels being m the total number of them and $[\cdot]_s$ denotes the element of the vector corresponding to the sth voxel. Finally, θ_0 is the initial guess for the parameters and P_0 its covariance matrix, which are assumed given. The scalar $\sigma_z > 0$ corresponds to the standard deviation of the measurement noise on Z^k. However, this is generally an unknown quantity, since it depends on the voxel size, *venc* and other MRI scan setup choices. But if we assume a known initial condition—which of course does not depend on the uncertain parameters θ—σ_z can be estimated by maximizing the likelihood of observing the measurements [28] at t^0 given $\mathbf{u}^0$ leading to

$$\sigma_z^2 \approx \frac{1}{m}\sum_{s=1}^{m}([Z^0 - \mathcal{H}(\mathbf{u}^0)]_s)^2. \tag{12}$$

In case that $\mathbf{u}^0 = \mathbf{0}$, σ_z becomes simply the standard deviation of the measurements at t^0.

4.3. The new inverse problem accounting for aliasing

As introduced in section 3.1, let us start with a single velocity measurement, for instance at one voxel of the image and one time instant. Assuming that the measurements M^u_{meas} are perturbed with zero-mean Gaussian noise, the estimation of u_{meas} without using equation (9) from the beginning, can be formulated as the solution of a least-squares estimation problem:

$$\arg\min_u J(u) \tag{13}$$

with

$$\begin{aligned} J(u) \equiv{}& \frac{1}{2\sigma_M^2}\left(\Re(M^u_{\text{meas}}) - |M^u_{\text{meas}}|\cos\left(\angle M^0_{\text{meas}} + u\frac{\pi}{venc}\right)\right)^2 \\ &+ \frac{1}{2\sigma_M^2}\left(\Im(M^u_{\text{meas}}) - |M^u_{\text{meas}}|\sin\left(\angle M^0_{\text{meas}} + u\frac{\pi}{venc}\right)\right)^2 \\ ={}& \frac{|M^u_{\text{meas}}|^2}{\sigma_M^2}\left(1 - \cos\left(\frac{\pi}{venc}(u_{\text{meas}} - u)\right)\right) \end{aligned} \tag{14}$$

with $\sigma_M > 0$ denoting the standard deviation in the measurement of the magnetization components. Note that to obtain formula (14) standard trigonometric identities were used.

Problem (13) has multiple solutions due to the periodicity of the cosine function, namely the set

$$\mathcal{U} = \{u_{\text{meas}} + 2j \cdot venc,\ \ j \in \mathbb{Z}\}$$

and hence formula (9) corresponds to the particular case $j = 0$. Figure 5 shows examples of the functions $J(u)$ for different values of $u_{\text{true}}/venc$, where those multiple solutions can be seen.

When $|venc| < |u_{\text{true}}|$, the un-aliased velocity value is still an element of the set $\mathcal{U}$, and therefore finding it requires either more information to find j and/or to restrict the search within that set.

In [29, 30], the un-aliased values were found by including additional measurements with different *venc* values.

In this work, we will however proceed by constraining the search by stating that the velocity at each measurement point depends on the same parameter set θ, where $\dim\theta \ll m$. Specifically, the measured (aliased) velocities are modeled by the reference solution detailed in the previous section.

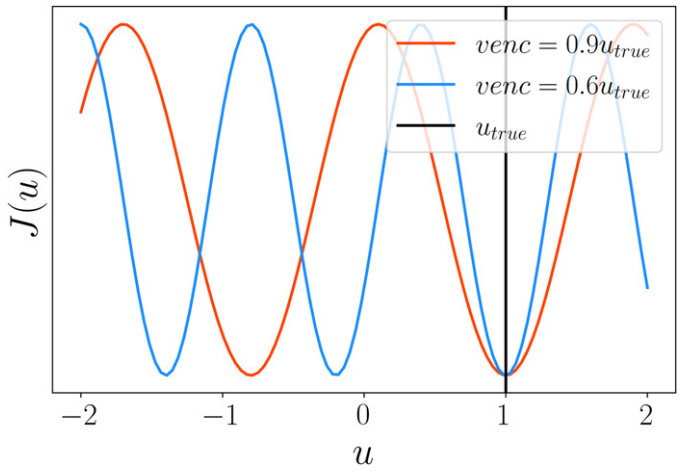

Figure 5. Cost function $J(u)$ for different values of *venc*.

Let us consider first a simple example: a *Poiseuille* solution for a flow in an infinite cylindrical pipe. Note that in this case, the velocity is modeled by $u_s = \theta \cdot a_s$, where a_s represents an unitary parabola shape at the sth measured voxel and θ the actual amplitude of the velocity profile. The parameter θ is then estimated by minimizing the next total function composed by the sum of m cost functions:

$$\arg\min_{\theta} \sum_{s=1}^{m} \frac{|M^u_{\text{meas, s}}|^2}{\sigma_M^2} \left(1 - \cos\left(\frac{\pi}{venc}(u_{\text{meas, s}} - \theta \cdot a_s)\right)\right). \tag{15}$$

Note that functions with different frequencies $\pi \cdot a_1/venc, \ldots, \pi \cdot a_m/venc$ are added, what is depicted in figure 6 for the Poiseuille example. This leads to the true value of θ becoming the global minimum and therefore, if starting a minimization procedure close enough, the true parameter can be identified even in the case that aliasing is present.

In the general case for the fluid flow parameter estimation problem, we will formulate the optimization problem as:

$$\hat{\theta} = \arg\min_{\theta} \frac{1}{2}\|\theta - \theta_0\|^2_{P_0^{-1}} + \frac{1}{\sigma_M^2} \sum_{k=1}^{N} \sum_{s=1}^{m} |M_s(t^k)|^2 \left(1 - \cos\left(\frac{\pi}{venc} \cdot \left([Z^k - \mathcal{H}(\mathbf{u}^k_\theta)]_s\right)\right)\right) \tag{16}$$

with Z^k the same (possibly aliased) velocity measurements vector as in the previous section and $|M_s(t^k)|$ the magnetization module at the sth voxel and kth timestep. Again, $\mathbf{u}^k_\theta$ and θ are related through the forward model summarized in algorithm 1.

Since σ_M depends also on the setup of the MRI scan, we assume that a perfectly known initial condition leads to the estimate:

$$\sigma_M^2 \approx \frac{1}{m} \sum_{s=1}^{m} |M_s^0|^2 \left(1 - \cos\left(\frac{\pi}{venc} \cdot \left([Z^0 - \mathcal{H}(\mathbf{u}^0)]_s\right)\right)\right). \tag{17}$$

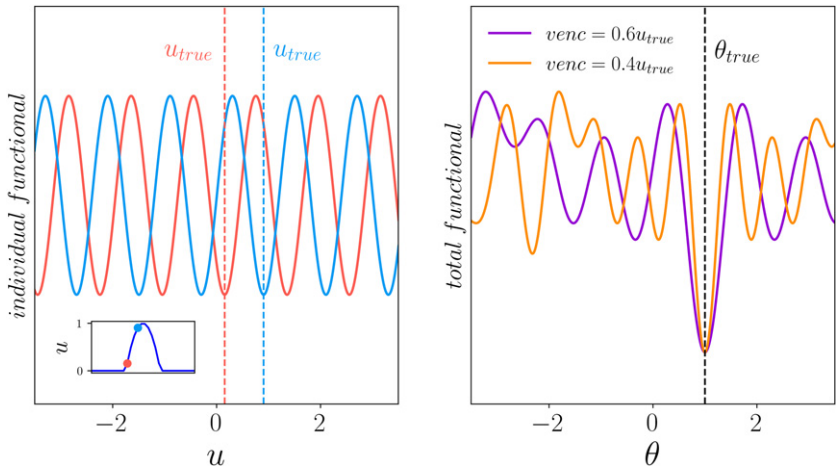

Figure 6. Left: independent cost functions for two voxels and same *venc*. Right: combined for all voxels in the Poseuille flow example.

It is worth noticing that by doing a second order Taylor expansion of expression (17) for $[Z^0]_s \approx [\mathcal{H}(\mathbf{u}^0)]_s$ (e.g. in case of large *venc*) one obtains

$$\sigma_M^2 \approx \frac{1}{m}\sum_{s=1}^{m} |M_s^0|^2 \frac{\pi^2}{2venc^2}\left([Z^0 - \mathcal{H}(\mathbf{u}^0)]_s\right)^2$$

and comparing it with equation (12) and assuming $|M_{\text{meas, 1}}| \approx \ldots \approx |M_{\text{meas, m}}| \equiv |\bar{M}|$, it leads to the relation:

$$\sigma_z \approx \frac{\sqrt{2}venc}{\pi}\sigma_M |\bar{M}|^{-1} \tag{18}$$

which is well known in phase-contrast MRI [6] and is aligned with the description in section 3.1.

Remark 1. Problem (16) is directly solvable with data that is already widely clinically available since clinical scanners also output the magnitude images as their standard setup.

Remark 2. The formulation in problem (16) allows for a straightforward extension to measurement sets with different *venc* values by generalizing the data fidelity term to:

$$\frac{1}{\sigma_M^2}\sum_{g=1}^{G}\sum_{k_g=1}^{N_{T,g}}\sum_{s_g=1}^{m_g} |M_{s_g}(t^{k_g})|^2\left(1 - \cos\left(\frac{\pi}{venc_g}\cdot\left([Z_g^{k_g} - \mathcal{H}_g(\mathbf{u}_\theta^k)]_{s_g}\right)\right)\right)$$

where the index g denotes the measurement—possibly with different spatio-temporal sampling—data set g taken with velocity encoding $venc_g$.

Table 2. Estimated standard deviations for the measurements.

	$venc = 115$ cm s^{-1}	$venc = 67$ cm s^{-1}	$venc = 28$ cm s^{-1}
σ_z (cm s^{-1})	9.16	5.22	2.21
σ_M (A cm^{-1})	0.0180	0.0176	0.0181

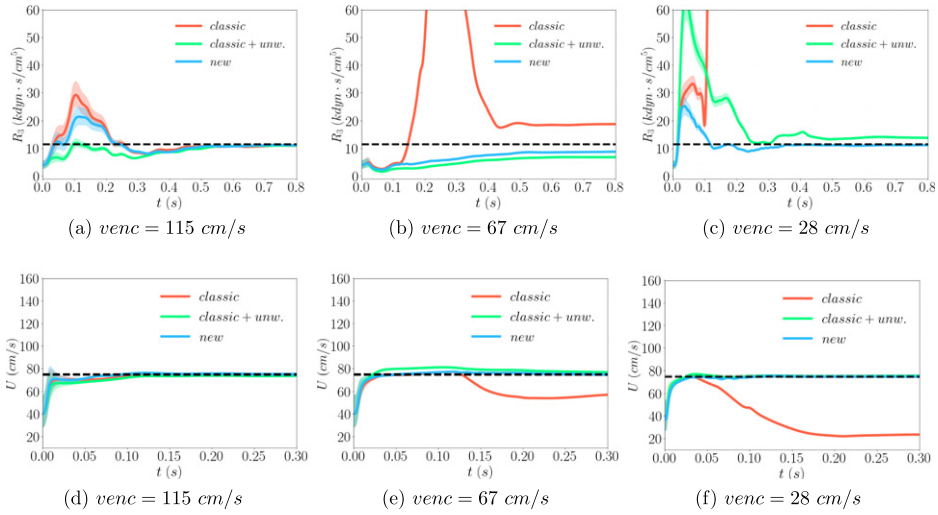

(a) $venc = 115\ cm/s$ (b) $venc = 67\ cm/s$ (c) $venc = 28\ cm/s$

(d) $venc = 115\ cm/s$ (e) $venc = 67\ cm/s$ (f) $venc = 28\ cm/s$

Figure 7. Estimated parameters over time for the initial guess I.

4.4. The sequential parameter estimator

Problems (11) and (16) can be solved by any optimization method. In this work, we chose a reduced-order unscented Kalman filter (ROUKF) [31], which has been successfully employed in blood flow problems [5, 32–35] presenting a computationally tractable way to deal with large time dependent PDE models as the one used here.

The ROUKF algorithm, detailed in appendix A, has three main steps:

(a) **Sampling:** for every time step t^n, $n > 0$ a number of *particles*, i.e., a deterministic perturbations of state and parameters is generated from the estimate at t^{n-1};

(b) **Prediction:** the forward solver is applied to each particle, so a new state at t^n is generated for each particle;

(c) **Correction:** an estimate of state and parameters is computed at t^n by combining the propagated particles and the measurements at t^n.

Correctly defining the state of the discrete dynamical system under consideration is of great importance in Kalman filtering. In the time-continuous case, it is evident that the state is $(\mathbf{u}, \pi_1, \ldots, \pi_K)$, i.e. the variables to which time derivatives are applied. In the time-discrete case in algorithm 1 the discrete state at time step t^n results in: $(\mathbf{u}^n, \pi_1^n, \ldots, \pi_K^n)$. All the other variables in the problem like $\tilde{\mathbf{u}}^n$ and p^n are internal quantities of the algorithm and are uniquely defined by the a given state.

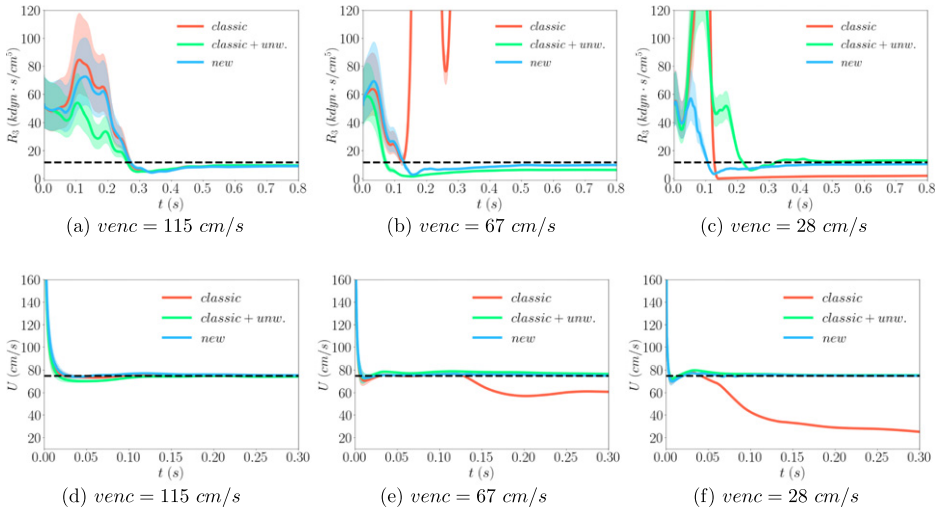

(a) $venc = 115\ cm/s$ (b) $venc = 67\ cm/s$ (c) $venc = 28\ cm/s$

(d) $venc = 115\ cm/s$ (e) $venc = 67\ cm/s$ (f) $venc = 28\ cm/s$

Figure 8. Estimated parameters over time for the initial guess II.

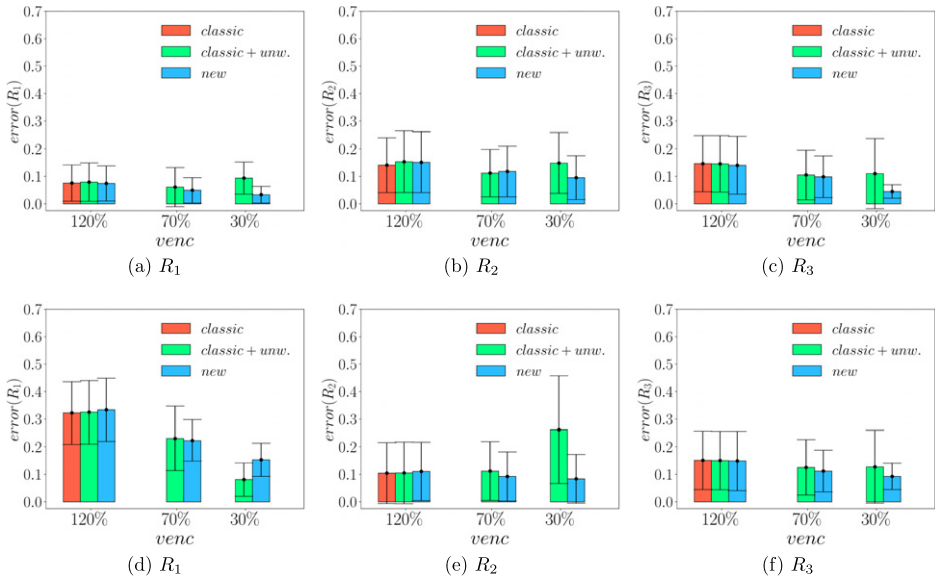

(a) R_1 (b) R_2 (c) R_3

(d) R_1 (e) R_2 (f) R_3

Figure 9. Final recovered resistances errors by each method for both initial guesses: I, upper row, and II, bottom row.

In Kalman filtering, the correction step relies on the so called measurement error or *innovation* Γ^n. In the case of problem (11), that is defined as [31]:

$$[\Gamma^n]_s \equiv [Z^n - \mathcal{H}(\mathbf{u}^n)]_s. \tag{19}$$

If a measurement Z^n is not available at the simulation time step t^n, then it is obtained by linear interpolation from the closest time steps where measurements are available.

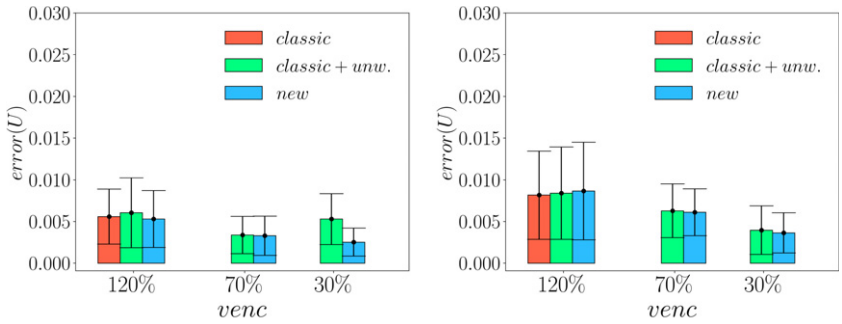

(a) Initial guess I (b) Initial guess II

Figure 10. Final recovered velocity amplitudes errors by each method for both initial guesses.

In order to derive the innovation for problem (16) we will proceed as follows. Since the innovation needs to be proportional to the derivative of the data-discrepancy term in the cost function [36], we know that the dependency will be with a sine function. Moreover, since problems (11) and (16) are equivalent when the *venc* is large and the magnitude is constant over the voxels, we require equation $(21d)_5$ (see appendix A) be the same for both problems in that scenario. Therefore, using relation (18) and a second order Taylor expansion for the functional in (16), we define the innovation for the Kalman filter in problem (16) as:

$$[\Gamma^n]_s \equiv \frac{1}{\sqrt{2}}|M_s(t^n)| \sin\Big(\frac{\pi}{venc} \cdot ([Z^n - \mathcal{H}(\mathbf{u}^n)]_s)\Big). \tag{20}$$

Last but not least, in order to ensure the positivity of the physical parameters to be optimized, a reparametrization was performed as previously done in several works [5, 32–35]. Denoting the physical parameters as β, the ROUKF is applied on θ such that $\beta = 2^\theta$.

4.5. Numerical experiments

We defined two sets of experiments starting from different initial guesses for the physical parameters to estimate:

- Initial guess I: $U = 40$, $(R_{d,1}, R_{d,2}, R_{d,3}) = (4000, 4000, 4000)$
- Initial guess II: $U = 250$, $(R_{d,1}, R_{d,2}, R_{d,3}) = (52\,500, 52\,500, 52\,500)$

Recall that the target values are $U = 75$, $(R_{d,1}, R_{d,2}, R_{d,3}) = (7200, 11\,520, 11\,520)$ as detailed in section 2.3. Here, the velocity amplitude U is in cm s^{-1} and the distal resistances $R_{d,i}$ are in (dyn · s)/cm^5.

The weights for the parameters for the ROUKF were taken as follows. An initial standard deviation of $P_0 = 0.5\mathbb{I}$ was set for the reparametrized parameters. This corresponds to a probability of 95% that the true parameters lie within the range half and double of the initial guess. On the other hand, for the measurements, assuming it at the initial time step mostly dominated by noise, the initial measured velocity and magnetization were used for computing the initial standard deviations σ_z and σ_M respectively, see table 2.

Figures 7 and 8 show the time evolution of the mean (thick line) and the standard deviation (as the shaded region) of the distal resistance R_3 and the inflow amplitude U during Kalman

filtering for initial guesses for the parameters I and II, respectively, and for the different *venc* values. The three methods are compared together: the classical formulation with both: normal and unwrapped data (denoted as *classical* + *unw.*), and the new formulation. Note that using the classical cost function formulation, the estimation succeeds for the case with unaliased data but fails as soon as aliasing appears. In contrast, for the new formulation the results remain robust with respect to aliasing. Moreover, for the largest *venc* case results with both formulations are very similar, which occurs by construction as mentioned above. Note also that when decreasing the *venc*, the sensitivity over time of the reconstructed parameter is increased in the case of the new functional. The results are robust to the choice of the initial guess, even when starting with very large (unphysiological) values. Figures 9 and 10 show error bars with the mean and standard deviation of the relative error for the reconstructed resistances and velocity amplitudes by each method respectively. The errors were computed for 30 independent realizations of the noise in the measurements. The results are not shown in cases with aliased data using the classic method, due to the lack of convergence.

5. Conclusion

We proposed a new formulation for parameter estimation in fluid flow problems when the measurements correspond to phase-contrast MRI (possibly) aliased and noisy velocities. The formulation was derived directly from the model of the MRI magnetization. We also showed how a popular sequential approach can be applied to solve the inverse problem.

Numerical results show correct estimation of boundary condition parameters for velocity encoding ranges even at 30% of the maximal velocity of the problem and delivers more accurate results than first unwrapping and then estimating the parameters using the standard cost function. Therefore, the presented approach relaxes the requirements in clinical data when personalizing fluid flow models with no additional pre-processing steps when aliasing is present.

Future work should involve working with real MRI data. Although the concepts of this work are applicable to that case, the main challenge to address there would be the fluid-structure interaction effects. Specifically, an observation operator that accounts for domain mismatch needs to be developed. This topic is however out of the scope of the present article and will be considered in follow up research.

Acknowledgments

CB and ML acknowledge the funding from the European Research Council (ERC) under the European Union's Horizon 2020 Research and Innovation Programme (Grant Agreement No. 852544—CardioZoom).

Data availability statement

The data that support the findings of this study are available upon reasonable request from the authors.

Appendix A. The reduced-order unscented Kalman filter

Here we detail the ROUKF algorithm adapted from [31]. Let us first consider the notation $[Y(^*)]$ as the matrix with the column-wise collection of vectors $Y^{(1)}, Y^{(2)}, \ldots$.

Define the *simplex sigma-points* $I^{(i)},\dots,I^{(p+1)}\in\mathbb{R}^p$ given such that $[I^{(*)}]\equiv[I_p^{(*)}]\in\mathbb{R}^{p\times(p+1)}$ is computed recursively as [37, 38]

$$[I_1^{(*)}]=\begin{bmatrix}-\dfrac{1}{\sqrt{2\alpha}} & \dfrac{1}{\sqrt{2\alpha}}\end{bmatrix},\quad \alpha=\frac{1}{p+1},$$

and

$$[I_d^{(*)}]=\begin{bmatrix} & & & 0\\ & [I_{d-1}^{*}] & & \vdots\\ & & & 0\\ \dfrac{1}{\sqrt{\alpha d(d+1)}} & \cdots & \dfrac{1}{\sqrt{\alpha d(d+1)}} & \dfrac{-d}{\sqrt{\alpha d(d+1)}}\end{bmatrix},\quad 2\leqslant d\leqslant p.$$

We denote by $\hat{X}_n^-,\hat{X}_n^+\in\mathbb{R}^r$ *a priori* (model prediction) and *a posteriori* (corrected by observations) estimates of the true state $X_n\in\mathbb{R}^r$. In the semi-implicit coupled 3D–0D fractional step algorithm 1, the state consists in the velocity field $\mathbf{u}^n$ and the Windkessel pressures π_ℓ^n. Estimates of all unknown parameters are summarized by the corresponding *a priori* and *a posteriori* vectors $\hat{\theta}_n^-,\hat{\theta}_n^+\in\mathbb{R}^p$. The discretized forward model is written as $X_n=A_n(X_{n-1},\theta_{n-1})$, A_n denoting the model operator.

For given values of the initial condition $\hat{X}_0^+=X^0\in\mathbb{R}^r$, the initial expected value of the parameters $\hat{\theta}_0^+=\theta_0\in\mathbb{R}^p$ and its covariance matrix P_0, perform

- **Initialization:** initialize the sensitivities as

$$L_0^\theta=\sqrt{P_0}\ \text{(Cholesky factor)},\quad L_0^X=0\in\mathbb{R}^{r\times p},\quad U_0=P_\alpha\equiv\alpha[I^{(*)}][I^{(*)}]^\intercal. \tag{21a}$$

Then, for $n>0$:

- **Sampling:** generate $p+1$ particles from the current state and parameter estimates, i.e. for $i=s1,\dots,p+1$:

$$\begin{cases}\hat{X}_{n-1}^{(i)}=\hat{X}_{n-1}^{+}+L_{n-1}^{X}C_{n-1}^{\intercal}I^{(i)},\\ \hat{\theta}_{n-1}^{(i)}=\hat{\theta}_{n-1}^{+}+L_{n-1}^{\theta}C_{n-1}^{\intercal}I^{(i)}\end{cases} \tag{21b}$$

with C_{n-1} the Cholesky factor of U_{n-1}^{-1}.

- **Prediction:** propagate each particle with the forward model and compute an *a priori* state prediction:

$$\begin{cases}\hat{X}_n^{(i)}=A_n(\hat{X}_{n-1}^{(i)},\hat{\theta}_{n-1}^{(i)}),\quad \hat{\theta}_n^{(i)}=\hat{\theta}_{n-1}^{(i)},\quad i=1,\dots,p+1\\ \hat{X}_n^-=E_\alpha([\hat{X}_n^{(*)}])\equiv\alpha\displaystyle\sum_{i=1}^{p+1}\hat{X}_n^{(i)}\\ \hat{\theta}_n^-=E_\alpha([\hat{\theta}_n^{(*)}])\end{cases}. \tag{21c}$$

- **Correction:** compute *a posteriori* estimates based on measurements for state and parameters, using definitions (19) or (20) for the ith particle innovation $\Gamma_n^{(i)}$:

$$\begin{cases} L_n^X = \alpha[\hat{X}_n^{(*)}][I^{(*)}]^\intercal \\ L_n^\theta = \alpha[\hat{\theta}_n^{(*)}][I^{(*)}]^\intercal \\ L_n^\Gamma = \alpha[\Gamma_n^{(*)}][I^{(*)}]^\intercal \\ U_n = P_\alpha + (L_n^\Gamma)^\intercal W_n^{-1} L_n^\Gamma, \quad P_\alpha = \alpha[I^{(*)}][I^{(*)}]^\intercal \\ \hat{X}_n^+ = \hat{X}_n^- - L_n^X U_n^{-1} \left(L_n^\Gamma\right)^\intercal W_n^{-1} E_\alpha([\Gamma_n^{(*)}]) \\ \hat{\theta}_n^+ = \hat{\theta}_n^- - L_n^\theta U_n^{-1} \left(L_n^\Gamma\right)^\intercal W_n^{-1} E_\alpha([\Gamma_n^{(*)}]) \end{cases} \tag{21d}$$

  with $W_n = \sigma_z^2 \mathbb{1}$ and $W_n = \sigma_M^2 \mathbb{1}$ for problems (11) and (16), respectively.

ORCID iDs

Jeremías Garay https://orcid.org/0000-0002-8299-0487

References

[1] Peiró J and Veneziani A 2009 Reduced models of the cardiovascular system *Cardiovascular Mathematics: Modeling and Simulation of the Circulatory System* (*MS & A*) ed L Formaggia, A Quarteroni and A Veneziani (Berlin: Springer) pp 347–94
[2] Westerhof N, Lankhaar J-W and Westerhof B E 2009 The arterial Windkessel *Med. Biol. Eng. Comput.* **47** 131–41
[3] Fevola E, Ballarin F, Jiménez-Juan L, Fremes S, Grivet-Talocia S, Rozza G and Triverio P 2021 An optimal control approach to determine resistance-type boundary conditions from *in vivo* data for cardiovascular simulations (arXiv:2104.13284)
[4] Pant S, Fabrèges B, Gerbeau J-F and Vignon-Clementel I E 2014 A methodological paradigm for patient-specific multi-scale CFD simulations: from clinical measurements to parameter estimates for individual analysis *Int. J. Numer. Methods Biomed. Eng.* **30** 1614–48
[5] Arthurs C J, Xiao N, Moireau P, Schaeffter T and Alberto Figueroa C 2020 A flexible framework for sequential estimation of model parameters in computational hemodynamics *Adv. Model. Simul. Eng. Sci.* **7** 1–37
[6] Markl M, Frydrychowicz A, Kozerke S, Hope M and Wieben O 2012 4D flow MRI *J. Magn. Reson. Imaging* **36** 1015–36
[7] Soulat G, McCarthy P and Markl M 2020 4D flow with MRI *Annu. Rev. Biomed. Eng.* **22** 103–26
[8] Taylor C A and Draney M T 2004 *Annu. Rev. Fluid Mech.* **36** 197–231
[9] Brown R W, Cheng Y-C N, Mark Haacke E, Thompson M R and Venkatesan R 2014 *Magnetic Resonance Imaging: Physical Principles and Sequence Design* 2nd edn (New York: Wiley)
[10] Loecher M, Schrauben E, Johnson K M and Wieben O 2016 Phase unwrapping in 4D mr flow with a 4D single-step Laplacian algorithm *J. Magn. Reson. Imaging* **43** 833–42
[11] Untenberger M, Hüllebrand M, Tautz L, Joseph A A, Voit D, Merboldt K D and Frahm J 2015 Spatiotemporal phase unwrapping for real-time phase-contrast flow MRI *Magn. Reson. Med.* **74** 964–70
[12] Loecher M, Johnson K, Landgraf B and Wieben O 2011 4D gradient based phase unwrapping for pc-mr flow data *Proc. ISMRM* p 3284
[13] Urbina J *et al* 2016 Realistic aortic phantom to study hemodynamics using MRI and cardiac catheterization in normal and aortic coarctation conditions *J. Magn. Reson. Imaging* **44** 683–97

[14] Alastruey J, Xiao N, Fok H, Schaeffter T and Figueroa C A 2016 On the impact of modelling assumptions in multi-scale, subject-specific models of aortic haemodynamics *J. R. Soc. Interface* **13** 20160073
[15] Guermond J L, Minev P and Shen J 2006 An overview of projection methods for incompressible flows *Comput. Methods Appl. Mech. Eng.* **195** 6011–45
[16] Bertoglio C, Caiazzo A and Fernández M A 2013 Fractional-step schemes for the coupling of distributed and lumped models in hemodynamics *SIAM J. Sci. Comput.* **35** B551–75
[17] Bertoglio C *et al* 2018 Benchmark problems for numerical treatment of backflow at open boundaries *Int. J. Numer. Methods Biomed. Eng.* **34** e2918
[18] Bazilevs Y, Calo V M, Cottrell J A, Hughes T J R, Reali A and Scovazzi G 2007 Variational multiscale residual-based turbulence modeling for large eddy simulation of incompressible flows *Comput. Methods Appl. Mech. Eng.* **197** 173–201
[19] Irarrazaval P, Firoozabadi A D, Uribe S, Tejos C and Sing-Long C 2019 Noise estimation for the velocity in MRI phase-contrast *Magn. Reson. Imaging* **63** 250–7
[20] Dong J, Chen F, Zhou D, Liu T, Yu Z and Wang Y 2017 Phase unwrapping with graph cuts optimization and dual decomposition acceleration for 3D high-resolution MRI data *Magn. Reson. Med.* **77** 1353–8
[21] Bhalerao A, Westin C-F and Kikinis R 1997 Unwrapping phase in 3D mr phase contrast angiograms *CVRMed-MRCAS'97* ed J Troccaz, E Grimson and R Mösges (Berlin: Springer) pp 191–202
[22] Xiang Q-S 1995 Temporal phase unwrapping for cine velocity imaging *J. Magn. Reson. Imaging* **5** 529–34
[23] Barnhill E, Kennedy P, Johnson C L, Mada M and Roberts N 2015 Real-time 4D phase unwrapping applied to magnetic resonance elastography *Magn. Reson. Med.* **73** 2321–31
[24] Lee A T, Bruce Pike G and Pelc N J 1995 Three-point phase-contrast velocity measurements with increased velocity-to-noise ratio *Magn. Reson. Med.* **33** 122–6
[25] Schnell S *et al* 2017 Accelerated dual-venc 4D flow MRI for neurovascular applications *J. Magn. Reson. Imaging* **46** 102–14
[26] Carrillo H, Osses A, Uribe S and Bertoglio C 2019 Optimal dual-VENC unwrapping in phase-contrast MRI *IEEE Trans. Med. Imaging* **38** 1263–70
[27] Itoh K 1982 Analysis of the phase unwrapping problem *Appl. Opt.* **21** 2470
[28] Rossi R J 2018 *Mathematical Statistics: An Introduction to Likelihood Based Inference* (New York: Wiley)
[29] Carrillo H, Osses A, Uribe S and Bertoglio C 2018 Optimal dual-venc unwrapping in phase-contrast MRI *IEEE Trans. Med. Imaging* **38** 1263–70
[30] Herthum H, Carrillo H, Osses A, Uribe S, Sack I and Bertoglio C 2022 Multiple motion encoding in Phase-Contrast MRI: A general theory and application to elastography imaging *Med. Image Anal.* **78** 102416
[31] Moireau P and Chapelle D 2011 Reduced-order unscented Kalman filtering with application to parameter identification in large-dimensional systems *ESAIM: Control Optim. Calc. Var.* **17** 380–405
[32] Bertoglio C, Moireau P and Gerbeau J-F 2011 Sequential parameter estimation for fluid-structure problems. Application to hemodynamics *Int. J. Numer. Methods Biomed. Eng.* **28** 434–55
[33] Moireau P, Xiao N, Astorino M, Figueroa C A, Chapelle D, Taylor C A and Gerbeau J-F 2012 External tissue support and fluid-structure simulation in blood flows *Biomech. Model. Mechanobiol.* **11** 1–18
[34] Bertoglio C, Barber D, Gaddum N, Valverde I, Rutten M, Beerbaum P, Moireau P, Hose R and Gerbeau J-F 2014 Identification of artery wall stiffness: *in vitro* validation and *in vivo* results of a data assimilation procedure applied to a 3D fluid-structure interaction model *J. Biomech.* **47** 1027–34
[35] Nolte D and Bertoglio C 2019 Reducing the impact of geometric errors in flow computations using velocity measurements *Int. J. Numer. Methods Biomed. Eng.* **35** e3203
[36] Moireau P, Chapelle D and Tallec P L 2009 Filtering for distributed mechanical systems using position measurements: perspectives in medical imaging *Inverse Problems* **25** 035010–35
[37] Pham D-T, Verron J and Gourdeau L 1998 Filtres de Kalman singuliers évolutifs pour l'assimilation de données en océanographie *C. R. Acad. Sci. IIA* **326** 255–60
[38] Hoteit I, Pham D-T and Blum J 2002 A simplified reduced order Kalman filtering and application to altimetric data assimilation in Tropical Pacific *J. Mar. Syst.* **36** 101–27